**ADVANCED
FUNCTIONAL
MATERIALS**

Supporting Information

Inducing and Probing Localized Excitons in Atomically Thin Semiconductors via Tip-Enhanced Cavity-Spectroscopy

Hyeongwoo Lee, Inki Kim, Chulho Park, Mingu Kang, Jinseong Choi, Kwang-Yong Jeong, Jungho Mun, Yeseul Kim, Jeonghoon Park, Markus B. Raschke, Hong-Gyu Park, Mun Seok Jeong, Junsuk Rho,* and Kyoung-Duck Park*

Supporting Information

Inducing and probing localized excitons in atomically thin semiconductors via tip-enhanced cavity-spectroscopy

Hyeongwoo Lee[†], Inki Kim[†], Chulho Park, Jinseong Choi, Mingu Kang,

Kwang-Yong Jeong, Jungho Mun, Yesul Kim, Jeong Hoon Park, Markus B. Raschke,

Hong-Gyu Park, Mun Seok Jeong, Junsuk Rho[*], and Kyoung-Duck Park[*]

H. Lee, J. Choi, M. Kang, Prof. K.-D. Park[*]
Department of Physics, Ulsan National Institute of Science and Technology
(UNIST), Ulsan 44919, Republic of Korea
[*]Email Address: kdpark@unist.ac.kr

I. Kim, Y. Kim, J. H. Park, Prof. J. Rho[*]
Department of Mechanical Engineering, Pohang University of Science and Technology
(POSTECH), Pohang 37673, Republic of Korea
[*]Email Address: jsrho@postech.ac.kr

J. Mun, Prof. J. Rho
Department of Chemical Engineering, Pohang University of Science and Technology
(POSTECH), Pohang 37673, Republic of Korea

C. Park, Prof. M.S. Jeong
Department of Energy Science, Sungkyunkwan University (SKKU), Suwon 16419, Republic
of Korea

K.-Y. Jeong, H.-G. Park
Department of Physics, Korea University, Seoul 02481, Republic of Korea.

Prof. M. B. Raschke
Department of Physics, Department of Chemistry, and JILA, University of Colorado, Boulder,
CO 80309, USA

RESONANCE OPTICL PROPERTIES OF THE BOWTIE ANTENNA

Scattering or absorption spectrum can be easily obtained experimentally for an array of plasmonic cavities or antennas, but it is a quite challenging measurement for a single cavity or antenna due to the difficulty of making a tight beam focus with the white light. Therefore, we measured a near-field scattering-absorption spectrum for a single bowtie antenna through near-field scanning optical microscope (NSOM) [see previous publication, Kim et al., *Mater. Today* **39**, 89 (2020)]. This scattering resonance is matched well with the simulated resonance wavelength of the bowtie nano-cavity.[1] Since we used an excitation laser with a wavelength of 632.8 nm, we used the bowtie nano-antennas having a tip angle of ~60° for resonance excitation effect. Note that other geometrical parameters (length, gap, RoC) of the bowtie antenna have little effect to the plasmon resonance.[1]

CALCULATION OF STRAIN MAP OF A WSe₂ ML ON THE BOWTIE STRUCTURE
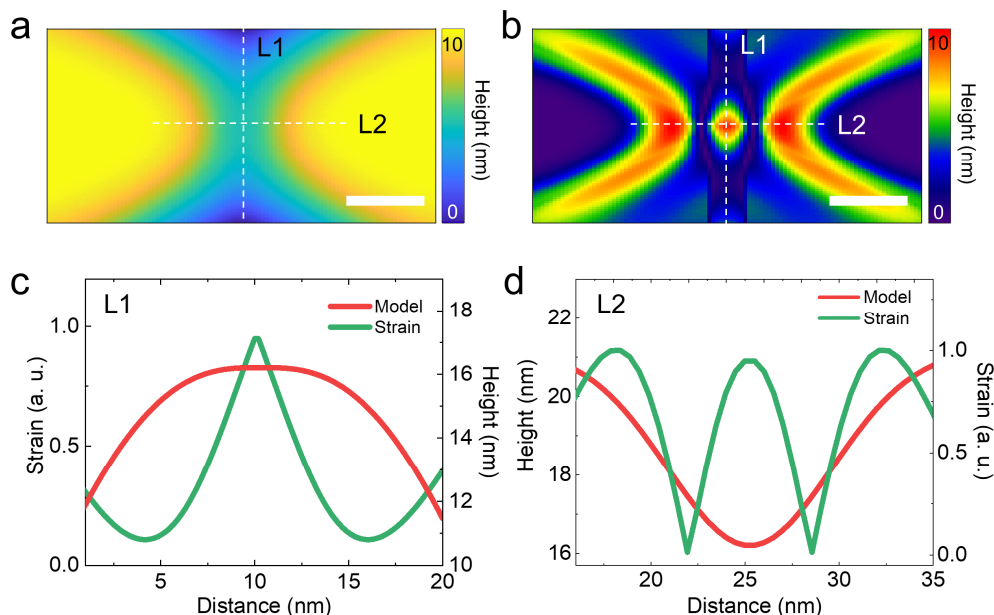
Figure S1. Modeled morphology (a) and strain map (b) of the WSe₂ monolayer on the bowtie antenna based on the measured AFM topography derived from Figure 3e and f. Scale bar is 10 nm. Line profile of the modeled morphology and calculated strain along the transverse line L1 (c) and longitudinal line L2 (d).

To quantify an anisotropic strain profile in the bowtie structure, we modeled a morphology of the WSe₂ monolayer on the bowtie structure (Figure S1a) based on the measured AFM topography (Figure 3e). We then calculate the strain map from the morphology using continuum theory for a thin and elastic 2D sheet (Figure S1b). Although we failed in TEPL imaging along the transverse direction, indeed, we expect sharp confined potential at the center of the nano-gap from the calculated strain map (Figure S1c). Whereas, this simulated strain result shows the potential well elongation along the longitudinal axis of the bowtie structure (Figure S1d). Note that we have tried TEPL scanning along the transverse direction many times, but we failed to obtain high resolution TEPL images due to the experimental difficulty. When the Au tip scanned over the edge or nano-gap structures from the Si substrate, the Au tip was always damaged since the height of the bowtie antenna is ~50 nm, i.e., the fragile Au tip (soft metal) with shear-force mode AFM is not appropriate to scan the step edge with a height of several tens of nanometers. Hence, to obtain TEPL image along the longitudinal axis (Figure 3a), we carefully located the Au tip onto the bowtie surface and tried TEPL scanning.
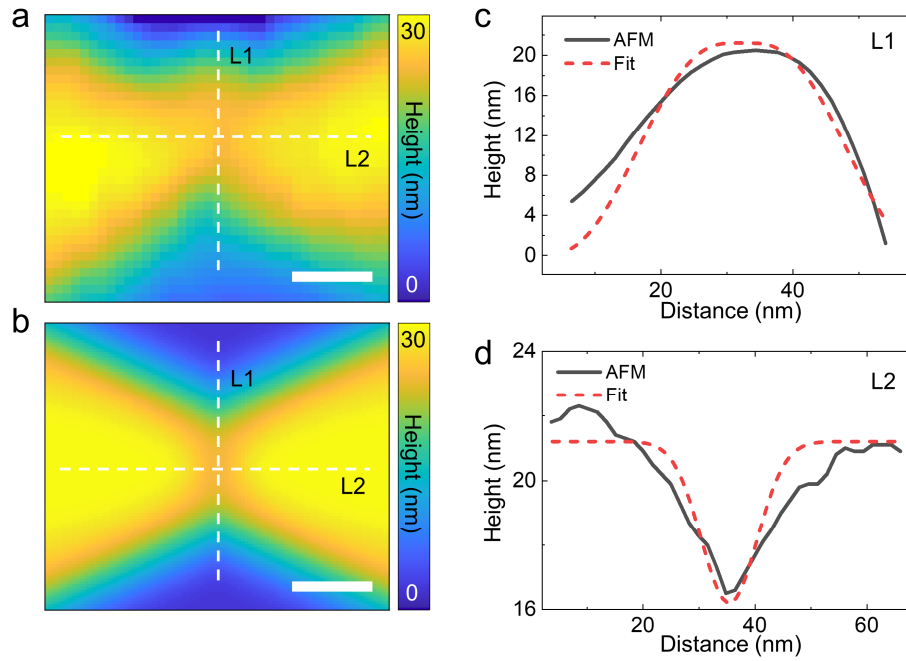
Figure S2. (a) AFM topography of the WSe$_2$ monolayer on the bowtie structure. (b) Modeled morphology for the AFM topography (a) to calculate the strain map. Scale bar is 15 nm. Line profiles of the measured AFM topography (black) and modeled morphology (red) across (c, L1) and along (d, L2) the bowtie structure.

CALCULATION OF TEPL ENHANCEMENT FACTOR

For our experimental result of a WSe$_2$ monolayer (Figure 3c), we can use the following equation for estimating TEPL enhancement factor (EF) of the neutral excitons[2]:

$$\text{EF} = \left(\frac{I_{tip-in} - I_{tip-out}}{I_{tip-out}}\right) \times \frac{A_{FF}}{A_{NF}}$$

where I_{tip-in} refers to the PL peak intensity with the tip approached at the nano-gap (TEPL) and $I_{tip-out}$ refers to the PL peak intensity with the tip retracted and measured at Si substrate (far-field PL at Si). A_{FF} and A_{NF} indicate the PL measurement areas corresponding to the focused beam spot by an objective lens and the near-field excitation region formed by Au tip, respectively. The values of I_{tip-in} and $I_{tip-out}$ are derived from curve fitting by a Lorentzian function. The values of A_{FF} and A_{NF} are derived using a general equation for an area of a circle πr^2 by considering a radius $r_{FF} \simeq \left(\frac{\lambda}{2NA}\right) \times 1.5 \times \sqrt{2} = \sim 839.0$ nm (the empirical factor of 1.5 is used and $\sqrt{2}$ is attributed to 45 degree of tilted stage)[3] of the far-field laser spot and r_{NF} with half of the spatial resolution of the used Au tip, 7.5 nm (derived from Figure 2d). Using EF equation and the derived values from our experiment, we estimate the TEPL enhancement factor for the neutral excitons as high as $\sim 4.0 \times 10^4$. This derived TEPL enhancement factor is in good agreement with the theoretical estimation, as described in Figure 5 of the main text.
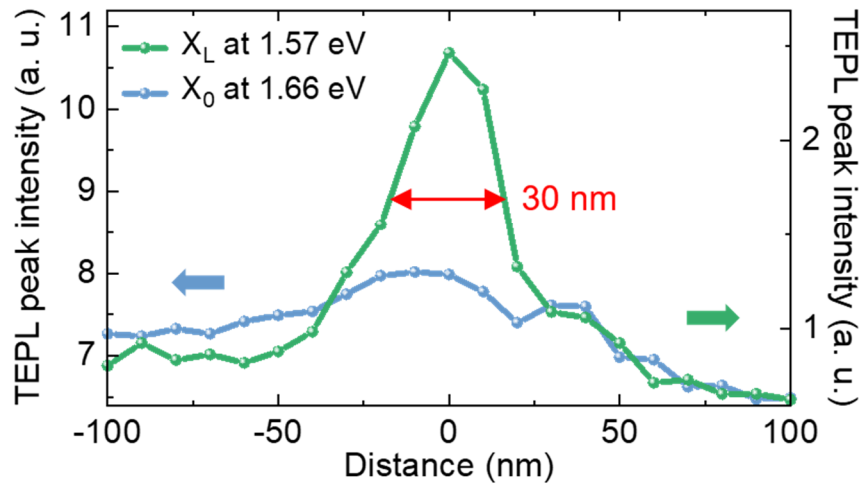
Figure S3. TEPL intensity profiles of X_0 (blue) and X_L (green) peaks, derived from the white dashed lines of Figure 3a in the main text, exhibiting the nanoscale spatial extent of radiative emission of the localized excitons.
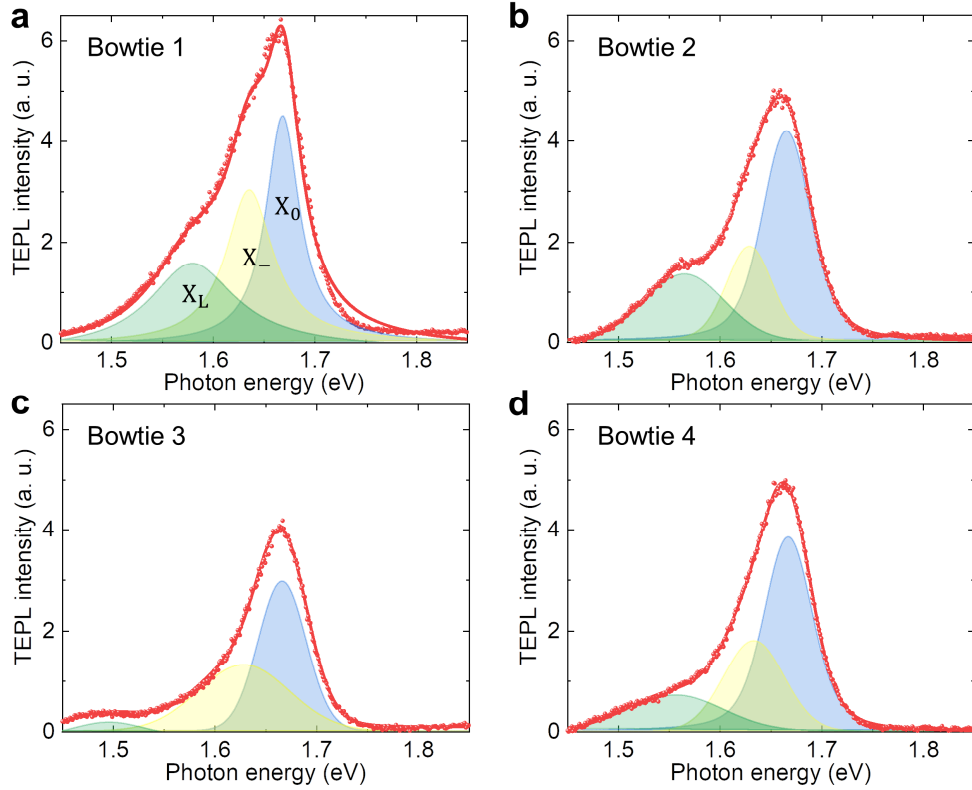
Figure S4. Observation of the X_L peak through TEPL spectroscopy at different bowtie antennas. TEPL spectrum (a) is derived from Figure 4a in the main text. TEPL spectra (b), (c), and (d) are obtained at the nano-gap of different bowtie antennas in the same condition as (a).

In this work, we deterministically induce localized exciton by using the triple-sharp-tips geometry. Figure S4 shows the deterministic generation of the localized exciton PL peak from different bowtie antennas to confirm the reproducibility of the proposed nano-cavity and -spectroscopy and the effect of the nano-gap width. Figure S4a is the TEPL spectrum derived from Figure 4a and Figure S4b-d are the TEPL spectra at different bowtie antennas with the nano-gap of ~5-20 nm. As can be seen in Figure S4a and b, when the tip is positioned on the relatively small nano-gap, the peak energy of the localized exciton emissions appears at higher energy due to the less confined potential[4,5] but the strong emission intensity caused from smaller mode volume is observed. In contrast, localized exciton emissions at the relatively lower energy with weaker emission intensity are observed in Figure S4c and d.
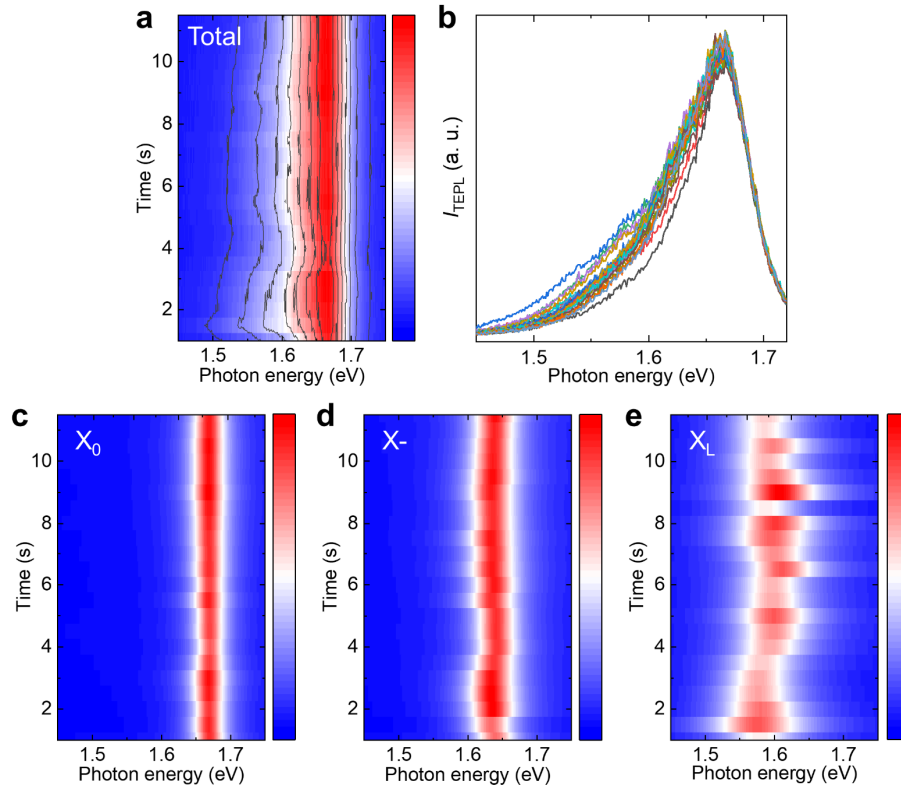
Figure S5. Original TEPL evolutions (a) and spectra (b) of the fitted time-series spectra in Figure 4b and d in the main text. X_0, X-, and X_L peaks are fitted by the Voigt line shape function and plotted with contour map in (c), (d), and (e), respectively.

Figure 3b and d in the main text are fitted results with the Voigt line shape function to clearly describe the TEPL evolution of the localized exciton peak and its different behavior compared to the neutral exciton peak. Figure S5a shows the evolution of original the TEPL spectra which including the neutral exciton, trion, and localized exciton peaks. The trion peak is observed near the neutral exciton peak with energy difference of ~16 meV and the localized exciton peak continuously appears at the lower energy states with its blinking behavior. It can be clearly seen in the collection of time-series TEPL spectra in Figure S5b. Figure S5c-e show contour plots of the neutral exciton, trion, and localized exciton peaks fitted with Voigt line shape function. The center wavelength for each peak is fixed with 500 iterations and average standard errors for fitting are ~0.2 nm, ~0.6 nm, and ~1.8 nm for X_0, X-, and X_L, respectively.
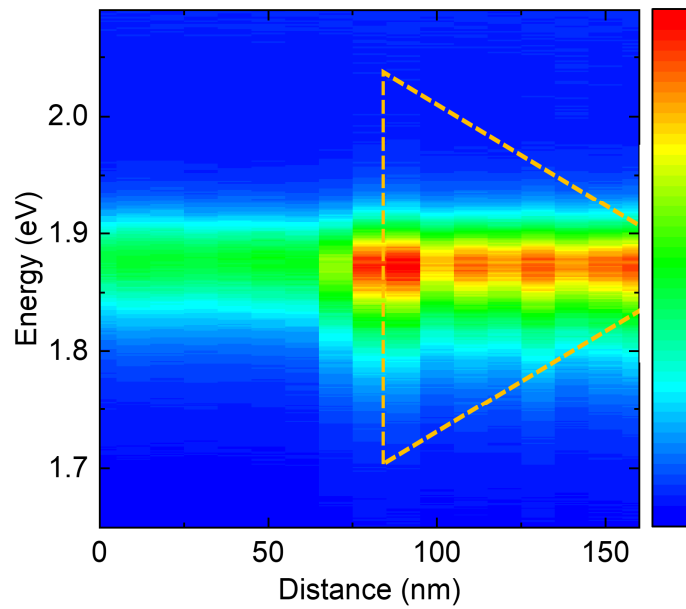
Figure S6. TEPL spectra of a WSe$_2$ monolayer when the Au tip scans the edge structure of the bowtie antenna.

In order to compare TEPL spectra of a WSe$_2$ monolayer for the different substrates (Si and Au), we show TEPL spectral line profile when the tip laterally moves from the Si substrate to Au substrate (bowtie antenna). When a plasmonic tip is placed on the metal substrate with a few nanometers gap, a larger field enhancement is obtained at the tip apex due to the dipole-dipole interaction, compared to the field enhancement of a plasmonic tip on the dielectric substrate[4]. Hence, Figure S6 shows a stronger TEPL signal at the Au surface, i.e., when the Au tip is placed on the surface of bowtie antenna. Furthermore, when the Au tip climbs the edge structure (at ~80 nm), we observe the strongest TEPL response since the direction of near-field polarization at the apex of Au tip is not normal direction with respect to the in-plane transition dipole moment of excitons.
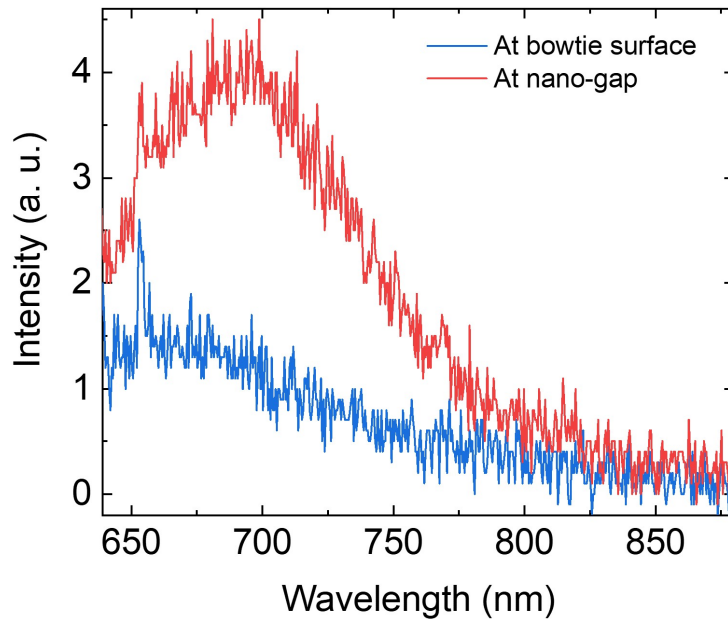
Figure S7. Spectra of near-field plasmon responses from the interaction between the bowtie antenna and Au tip without the WSe$_2$ crystal. Plasmon responses when the tip is located on the surface of bowtie antenna (blue) and nano-gap (red), respectively.

Before we transfer a WSe$_2$ monolayer onto the bowtie antenna, we measure tip-induced plasmon responses in the bowtie surface and the nano-gap, as shown in Figure S7. When the tip is located on the surface of bowtie antenna, plasmon intensity is relatively small. On the other hand, when the tip position is moved to the center of the nano-gap, the intensity enhancement and spectral redshift of gap plasmon peak are observed. These features exhibit the strong optical field localization by the triple-sharp-tips cavity structure[3, 7, 8].
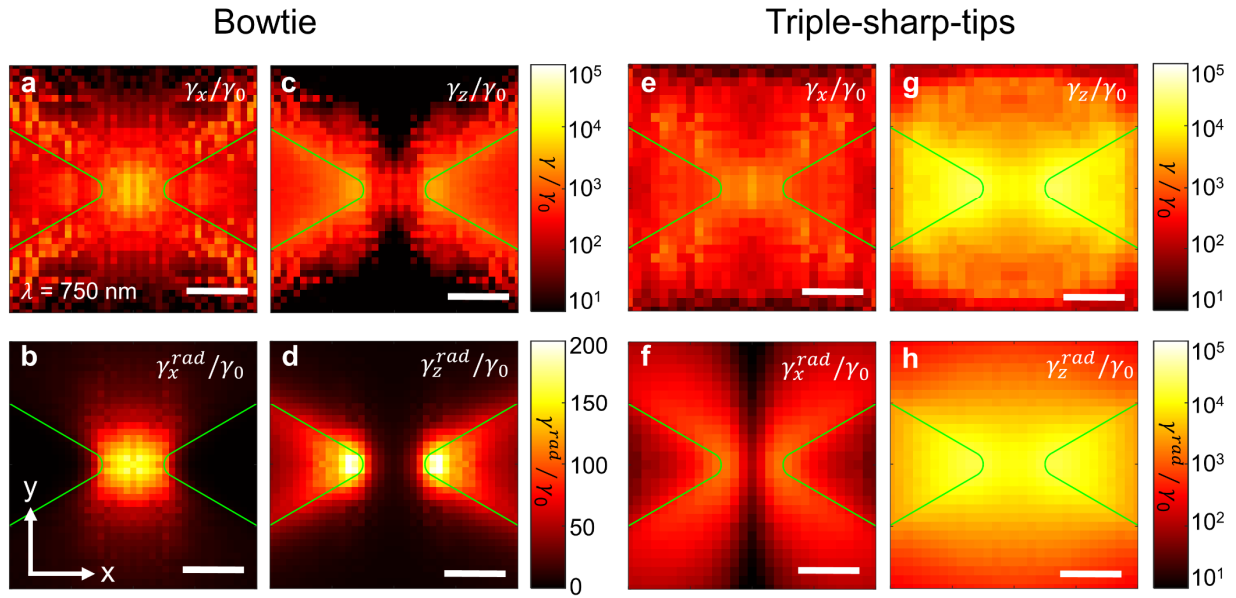
Figure S8. Simulated contour maps of the total-decay-rate for x-polarized dipole emitters (a) and z-polarized dipole emitters (c) at the bowtie antenna. Corresponding radiative-decay-rate contour maps for x-polarized dipole emitters (b) and z-polarized dipole emitters (d). Simulated contour maps of the total-decay-rate for x-polarized dipole emitters (e) and z-polarized dipole emitters (g) at the triple-sharp-tips cavity. Corresponding radiative-decay-rate contour maps for x-polarized dipole emitters (f) and z-polarized dipole emitters (h). In the simulations, the target wavelength is set to 750 nm (emission wavelength of WSe_2) and the contour plot plane is fixed 1.5 nm above the bowtie surface. Scale bar is 5 nm.

Figure 5i-l in the main text show the distributions of the radiative-decay-rate of dipole emitters at the bowtie antenna and the triple-sharp-tips cavity. In Figure S8, we show the total-decay-rate distribution to explain the clearer effect of the triple-sharp-tips geometry. Figure S8a shows that the total-decay-rate for x-polarized dipole emitters is high at the center of nano-gap. In addition, by the cavity effect of the bowtie antenna, the radiative-decay-rate for x-polarized dipole emitters is locally high at the nano-gap, as can be seen in Figure S8b. In contrast, the total-decay-rate for z-polarized dipole emitters is not distinctly high at the nano-gap (Figure S8c) and the radiative-decay-rate distribution is dispersed (Figure S8d). When we add Au tip on the nano-gap, the field concentration in the z-axis is dramatically increased. Thus, while the total-decay-rate (Figure S8e) and the radiative-decay-rate (Figure S8f) distributions for x-polarized dipole emitters look similar to the results of the bowtie antenna case, the total-decay-rate for z-polarized dipole emitters is highly increased with the additional tip effect, as can be seen in Figure S8g. Furthermore, we can figure out from Figure S8h that radiative-decay is dominant in the total-decay-rate. Regarding the distribution, the high radiative-decay-rate emitters are concentrated at the nano-gap, in contrast to the result of the bowtie antenna case (Figure S8d). Hence, this result demonstrates the highly efficient cavity effect of the triple-sharp-tips structure.
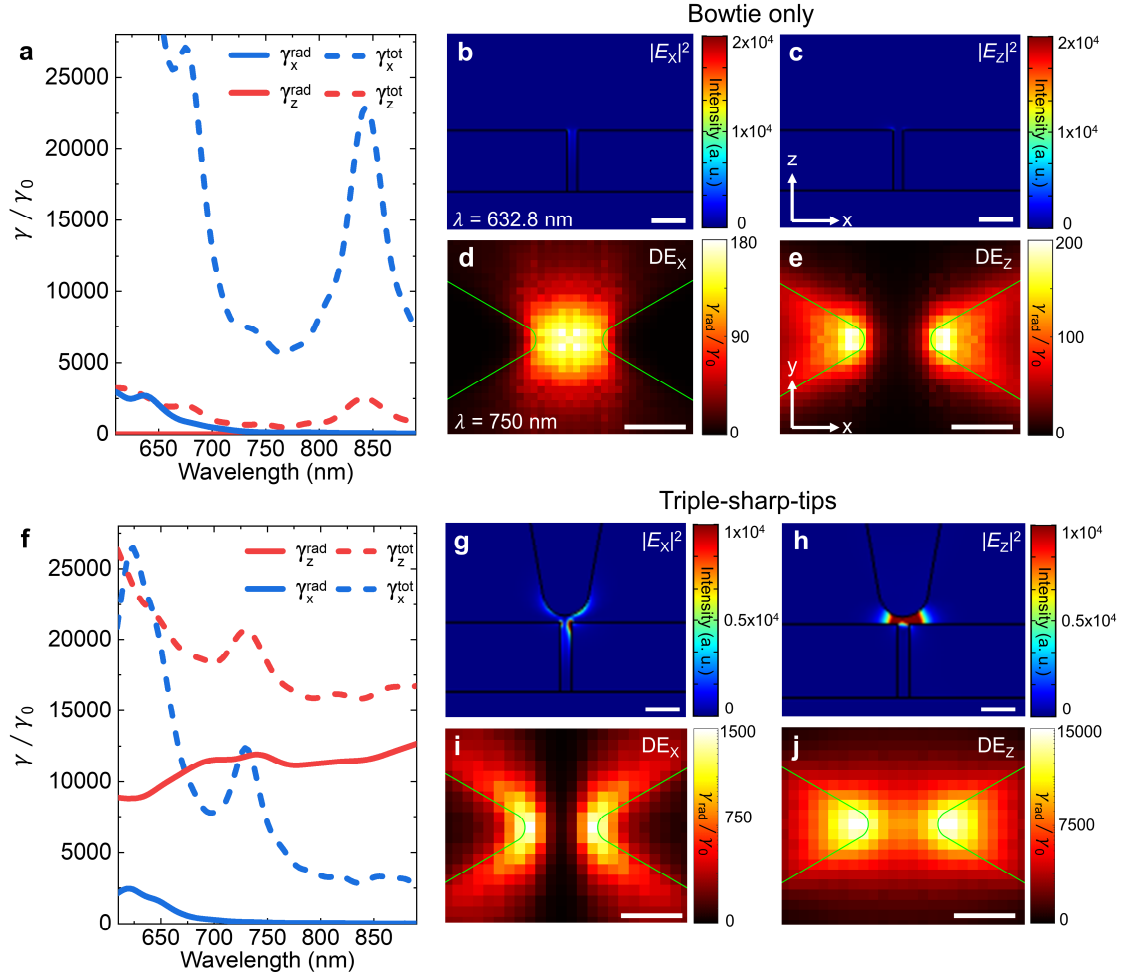
Figure S9. Electromagnetic simulation of the spatial optical properties in the triple-sharp-tips structure with the linear scale. (a, f) Simulated cross-sections for the enhancement of total (dashed lines) and radiative (solid lines) decay rates in the nano-gap of the bowtie antenna (a) and triple-sharp-tips (f) structure. The cross-sections are simulated for the x- (blue) and z-polarized (red) dipole emitters placed 1.5 nm above the top surface of the bowtie antenna. Simulated in-plane (b, g) and out-of-plane (c, h) optical field intensity distributions in the bowtie antenna (b, c) and the triple-sharp-tips (g, h) structure. The wavelength of the excitation beam is fixed to 633 nm and scale bars are 15 nm. Simulated radiative-decay-rate enhancement distributions in the bowtie antenna (d, e) and triple-sharp-tips (i, j) structure for x- (d, i) and z-polarized (e, j) dipole emitters placed 1.5 nm above the top surface of the bowtie antenna. The wavelength of emission is fixed to 750 nm and scale bars are 5 nm.

SIMULATION DETAILS AND CONSIDERATION OF THE PROPAGATING SPPs

As seen in Figure S10, the Au tip has a sufficiently large cone shape (2 μm height) with radius of curvature of 10 nm and tapering angle of 10°. The end of tip is located 3 nm above and the dipole is located 1.5 nm above from the bowtie tip. In this case, the propagating surface plasmon polaritons (SPP) along with the tip can affect to the radiative decay rate. As indicated in the reference,[9] a propagating SPP can have non-radiative decay rate, so that the power monitor surrounding bowtie system may include such non-radiative decay rate of SPP.[9] However, it is hard to rigorously calculate the amount of decay rate through the tip, though, we can see the field distributions of the system and confirm that such effect is negligible compared to strong gap plasmon resonance in the triple sharp tips. We conduct simple FDTD simulation to verify the claim. As seen in Figure S11, we set two power monitors near the bowtie structures (T_rad) and upper side of the Au tip (T_tip). The calculated power is normalized by space dipole radiation power. The field enhancement along the tip at 750 nm wavelength is negligible compared to that of hotspot. Also, as indicated in the reference,[9] if the distance between dipole and the tip is closed to 1 nm or below, the amount of non-radiative decay rate is much smaller than near field non-radiative decay rate (or local energy transfer).
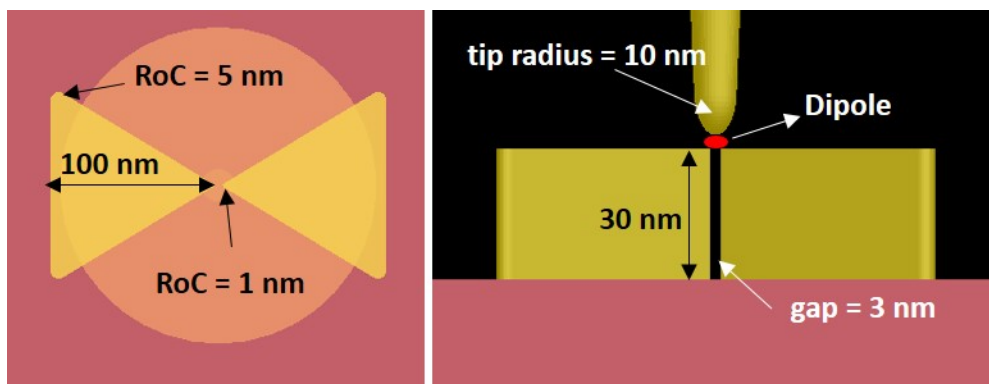
Figure S10. Geometric parameters for FDTD simulation.
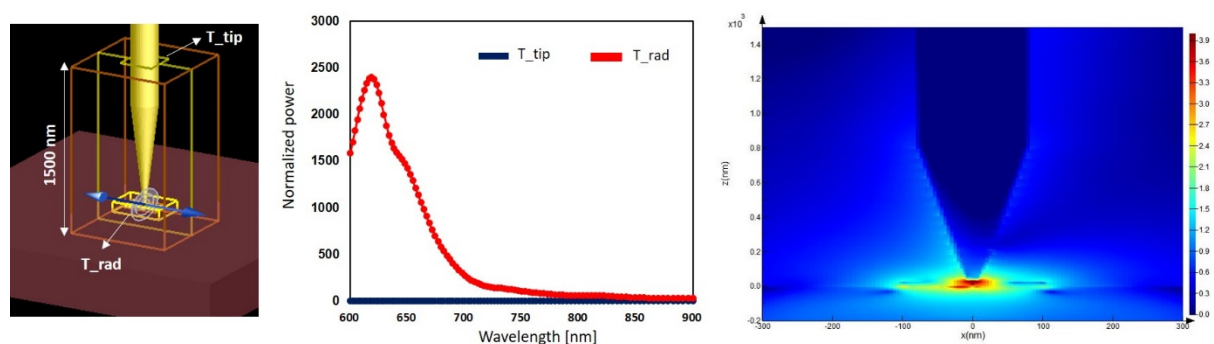
Figure S11. FDTD simulation schematic, calculated power and field distribution from a dipole source. The field distribution is plotted in logscale.

OBSERVATION OF LOCALIZED EXCITON AT LOW TEMPERATURE
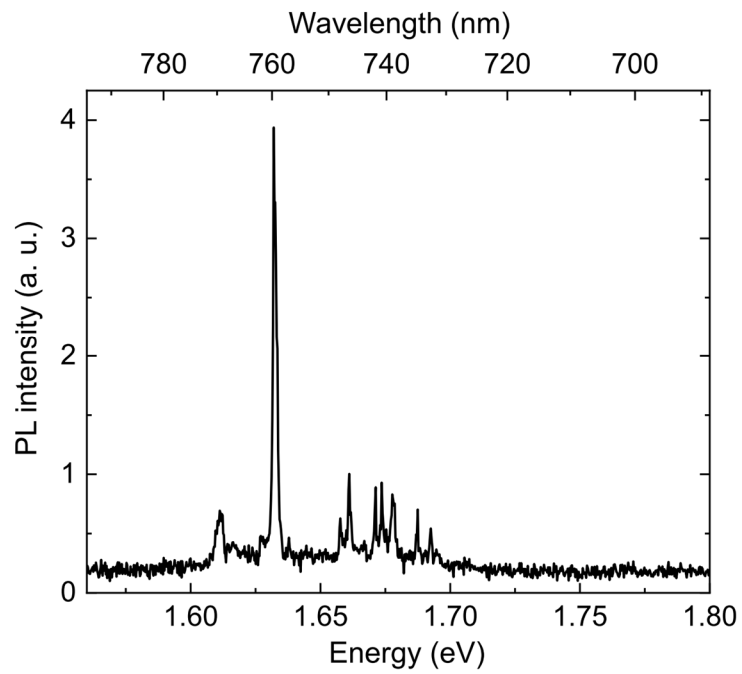
Figure S12. Observed PL spectrum of WSe$_2$ monolayer on the bowtie antenna.

To clarify the existence of X_L originated from the confinement potential of the bowtie antenna, we measure PL spectrum with confocal microscopy at 4K. As shown in Figure S12, sharp X_L emission peak at the low energy is observed from the bowtie antenna.

References

[1] Kim, I. et al., Cascade domino lithography for extreme photon squeezing. *Mater. Today* 39, 89 (2020).

[2] Stadler, J., Schmid, T. & Zenobi, R. Nanoscale chemical imaging using top-illumination tip-enhanced Raman spectroscopy. *Nano Lett.* **10**, 4514–4520 (2010).

[3] Kravtsov, V., Berweger, S., Atkin, J. M., & Raschke, M. B. Control of plasmon emission and dynamics at the transition from classical to quantum coupling. *Nano Lett.* **14**, 5270-5275 (2014).

[4] Darlington, T. P. et al., Imaging strain-localized excitons in nanoscale bubbles of monolayer WSe_2 at room temperature. *Nat. Nanotechnol.* **15**, 854-860 (2020).

[5] Kern, K. et al., Nanoscale Positioning of Single-Photon Emitters in Atomically Thin WSe_2. *Adv. Mater.*, **28**, 7101-7105 (2016).

[6] Nastaran K., Sylvain V., and François L., Localized enhancement of electric field in tip-enhanced Raman spectroscopy using radially and linearly polarized light. *Opt. Exp.* **21**, 25271-25276 (2013)

[7] Willets, K. A., & Van Duyne, R. P. Localized surface plasmon resonance spectroscopy and sensing. *Annu. Rev. Phys. Chem.* **58**, 267-297 (2007).

[8] Fromm, D. P., Sundaramurthy, A., Schuck, P. J., Kino, G., & Moerner, W. E. Gap-dependent optical coupling of single bowtie nanoantennas resonant in the visible. *Nano Lett.* **4**, 957-961 (2004).

[9] Issa, N. A., Guckenberger, R. Fluorescence near metal tips: The roles of energy transfer and surface plasmon polaritons. *Opt. Exp.* **15**, 12131-12144 (2007).